



Full Length Article

Fe₃Se₄ nanoparticles confined in hollow carbon nanocages for high-performance sodium-ion batteriesJiajia Ye^{a,b}, Zhiqiang Zheng^a, Guang Xia^a, Cheng Hu^{a,b,*}^a Key Laboratory for Liquid-Solid Structural Evolution and Processing of Materials (Ministry of Education), School of Materials Science and Engineering, Shandong University, Ji'nan 250061, Shandong, PR China^b Suzhou Institute of Shandong University, Suzhou 215123, Jiangsu, PR China

ARTICLE INFO

Keywords:
 Fe₃Se₄@C
 Nanocages
 Anodes
 Sodium-ion batteries

ABSTRACT

Fe₃Se₄ nanoparticles confined in hollow and self-supported carbon nanocages are synthesized for the first time through facile Fe₃O₄ nanospheres precursor etching couple with a following selenization process. The as-obtained Fe₃Se₄@C nanocages exhibit excellent sodium storage performance as sodium-ion battery anodes. The remarkable electrochemical properties are attributed to the high specific capacity of Fe₃Se₄ on top of the specially-designed nanocage architecture, in which the sufficient internal void space between the Fe₃Se₄ nanoparticles and the carbon shell accommodates the volume variation of Fe₃Se₄ to avoid and deforming the carbon shell as well as the entire composite nanostructure. The presence of the highly conductive carbon shells facilitate fast electron and Na⁺ ion transportation to promote continuous sodiation and desodiation. Benefiting from this unique nanostructure, the composite delivers a stable high specific capacity of 544.1 mAh g⁻¹ at 200 mA g⁻¹ after 100 charge/discharge cycles. Furthermore, a stable capacity of 402.2 mAh g⁻¹ is retained at 2000 mA g⁻¹ after 200 cycles. Meanwhile, a high specific capacity of 328.7 mAh g⁻¹ is achieved at the extraordinary current density of 5000 mA g⁻¹, manifesting an outstanding sodium storage performance.

1. Introduction

Sodium-ion batteries (SIBs) have attracted tremendous research attention and changed the landscape of electrochemical energy storage owing to their advantage of low cost resulted from the natural abundance of elemental sodium as compared with lithium [1]. However, Na⁺ ion possesses a larger radius (1.02 Å) that results in slower Na⁺ ion transportation, sluggish reaction kinetics, and greater volume change that significantly affects the structural stability of the electrodes during cell charge and discharge [2]. The major challenge for the development of SIBs anodes resides in designing robust anodes materials that well host Na⁺ ions with effective volume change buffering whilst providing fast Na⁺ ion transportation to enable enhanced reaction kinetics.

Various anode SIB anode materials have been proposed and investigated, including carbon-based materials [3,4], metal oxides (TiO₂ [5], and SnO₂ [6]), alloys (Sb [7], Sn [8], and P [9]) and selenides (CoSe_x [10,11], NiSe₂ [12], FeSe_x [13,14], MoSe₂ [15] and Cu₂Se [16]). Among these available anodes materials, metal selenides attracted much research efforts in view of their high theoretical capacity, enhanced electrochemical activity and appropriate working potentials

[12–15]. Iron selenides, in particularly, are considered as the most promising SIB anode materials due to their high theoretical capacity, good chemical stability and the rich abundancy of Fe resources [12,13]. However, the great volume variation and relatively low electrical conductivity of iron selenides leads to undesired electrochemical performance during repeated cycling. To resolve the above issues, nanostructured iron selenides such as nanoparticles [17], yolk-shells [18], nanoplates [19] and nanospheres [20] are designed and demonstrated. Delicate nanostructures provide improved specific surface area and abundant active sites for Na⁺ ion diffusion and storage. Besides, coupling with electrically conductive carbon have been employed as a popular approach to improve the structural stability and enable high electrical conductivity for active materials. Fan *et al.* prepared FeSe₂@C core-shell nanorods *via* a thermally-induced selenization process to deliver high reversible capacities [21]. Hollow FeSe₂/C nanospheres were reported by Lan *et al.* [22] to exhibit superior rating capability. Fe₃Se₄, as an important iron selenide, have however not yet been reported in the literature to our knowledge. Compared with other metal selenides that serve as SIB anodes, Fe₃Se₄ possesses a NiAs-type structure with iron vacancies arranged in an ordered fashion that provides more efficient active sites for Na⁺ ion insertion to enable high

* Corresponding author.

E-mail address: c.hu@sdu.edu.cn (C. Hu).

theoretical capacity [23]. Meanwhile, the monoclinic unit cell of Fe_3Se_4 ($a = 6.167 \text{ \AA}$, $b = 3.537 \text{ \AA}$, $c = 11.17 \text{ \AA}$, and $\beta = 92.0^\circ$) is able to effectively store multiple types of metal ion (such as Li^+ , Na^+ and K^+) [23]. It is therefore highly desirable to investigate the sodium storage performance of Fe_3Se_4 anodes by rational designing an appropriate nanostructure taking into account all of the above considerations.

In this work, we present a unique $\text{Fe}_3\text{Se}_4@\text{carbon}$ nanocages composite composed of Fe_3Se_4 nanoparticles confined in hollow carbon nanocages for the first time through a facile etching method coupled with a novel selenization strategy. Through confining Fe_3Se_4 nanoparticles in hollow carbon nanocages, this architectural provides synergistic improvements to resolve the problems associated with most SIBs anodes during the discharge/charge processes. The hollow carbon nano-shells act as self-supporting framework that effectively improves the electrical conductivity to facilitate electron transfer whilst prevents the agglomeration of the active materials. More importantly, the extra void space between the Fe_3Se_4 nanoparticles and carbon shells allows Fe_3Se_4 to expand freely whilst maintaining structural integrity. The as-synthesized $\text{Fe}_3\text{Se}_4@\text{C}$ NCs demonstrate a high reversible capacity of 455.6 mAh g^{-1} at 1000 mA g^{-1} after 200 charge/discharge cycles. The composite also exhibits remarkable rating performance of 330.6 mAh g^{-1} at a high rate of 5000 mA g^{-1} . The obtained specific capacity and cycling stability at this exceptionally high current density outperform most other anode materials reported in the literature.

2. Experimental

2.1. Sample preparation

Fe_3O_4 nanospheres were synthesized using a simple hydrothermal method. In a typical process, $1.35 \text{ g FeCl}_3\text{H}_2\text{O}$ and $3.6 \text{ g CH}_3\text{COONa}$ were added into $50 \text{ mL (CH}_2\text{OH)}_2$ under magnetic stirring to form a yellow solution. The resultant solution was then transferred to an autoclave, which was kept at 200°C for 8 h. The resulted sample was centrifuged and washed several times with DI water and ethanol, followed by drying in a vacuum oven at 70°C for 24 h for further use.

To prepare $\text{Fe}_3\text{O}_4@\text{C}$ core-shell nanospheres, polydopamine was first wrapped on the surface of the Fe_3O_4 nanospheres and then carbonized. 400 mg as-prepared Fe_3O_4 nanospheres were first dispersed into 200 mL of $20 \text{ mM Tris-buffer}$ solution by ultrasonication. 200 mg of dopamine hydrochloride was then added to the above dispersion, which was kept stirring for 24 h. The resultant product was collected via centrifugation and washed three times with deionized water and ethanol respectively before dried at 70°C overnight. The obtained $\text{Fe}_3\text{O}_4@\text{polydopamine}$ (PDA) was calcined at 550°C for 3 h in Ar atmosphere with a heating rate of 5°C min^{-1} to yield the $\text{Fe}_3\text{O}_4@\text{C}$ core-shell nanospheres.

To synthesize $\text{Fe}_3\text{Se}_4@\text{C}$ nanocages (denoted as $\text{Fe}_3\text{Se}_4@\text{C}$ NCs), as-obtained core-shell $\text{Fe}_3\text{O}_4@\text{C}$ nanospheres was first dispersed in $3 \text{ M hydrochloric acid (HCl)}$ solution and stirred continuously for 1–2 h at 25°C to partially etch the Fe_3O_4 . In the following selenization, 360 mg selenium powder (99.99 wt%) was loaded into an alumina boat in the upstream zone of a tube furnace with a following Ar atmosphere, while another boat containing $60 \text{ mg HCl-etched Fe}_3\text{O}_4@\text{C}$ nanospheres was put at the downstream. The temperature was elevated to 600°C and held for 3 h. For comparison, $\text{Fe}_3\text{Se}_4@\text{C}$ nanospheres (denoted as $\text{Fe}_3\text{Se}_4@\text{C}$ NSs) were synthesized following the same methods using unetched $\text{Fe}_3\text{O}_4@\text{C}$ core-shell nanospheres. Fe_3Se_4 nanospheres (denoted as Fe_3Se_4 NSs) were synthesized following the same methods by direct selenization of Fe_3O_4 nanospheres. Hollow carbon nanospheres (denoted as hollow C NSs) were synthesized by completely etching the Fe_3O_4 from $\text{Fe}_3\text{O}_4@\text{C}$ in $3 \text{ M hydrochloric acid (HCl)}$ solution for 2 h.

2.2. Sample characterization

Phase analysis of the prepared samples were performed by powder

X-ray diffraction (XRD, Bruker D8 Advance) using a Cu $\text{K}\alpha$ radiation source ($\lambda = 1.5418 \text{ \AA}$). X-ray photoelectron spectroscopy (XPS, Thermo ESCALAB 250XI) was employed to further confirm the valence states of elements in the as-prepared samples. Additionally, Raman spectroscopy was conducted on a HORIBA Jobin Yvon T64000 spectrometer using 532 nm laser. Surface morphology and chemical compositions were investigated by using scanning electron microscopy (SEM, JEOL JSM-6700F) and corresponding energy dispersive X-ray spectroscopy (EDS, Oxford INCA X-sight). Microstructure and corresponding elemental distribution were analysed on a JEM 2100F transmission electron microscope (TEM) equipped with an energy dispersive X-ray spectrometer (X-max 80 T, Oxford, UK). The TEM was operated at 200 kV . The fraction of Fe_3Se_4 by weight was determined by using a thermogravimetric analyzer (TGA, NETZSCH, TG 209, $10^\circ\text{C min}^{-1}$ to 950°C in air). Nitrogen adsorption and desorption measurements were performed at 77 K using a Micromeritics ASAP 2460 adsorption analyser.

2.3. Electrochemical measurements

CR2032 coin-type cells were assembled using sodium metal foils as counter and reference electrodes, glass microfiber filters (Whatman GF/D) as separators, and 1 M NaPF_6 in ethylene carbonate and diethyl carbonate (1:1 v/v, with 5 wt% FEC additive) as electrolyte. As prepared active materials (70%), Super P (20%), and sodium carboxyl methyl cellulose (10%) were mixed in water to form a homogeneous slurry and blade coated on Cu foils to form the working electrodes. Cell assembly was carried out in an argon filled glovebox (MIKROUNA, Super, $\text{O}_2 < 0.1 \text{ ppm}$, $\text{H}_2\text{O} < 0.1 \text{ ppm}$). The reported specific capacities herein is based on the entire mass of the composites of $\text{Fe}_3\text{Se}_4@\text{C}$ NCs, $\text{Fe}_3\text{Se}_4@\text{C}$ NSs, Fe_3Se_4 NSs as well as the hollow C NSs in the electrode, not the mass of Fe_3Se_4 only. Galvanostatic charge/discharge tests were performed on a NEWARE BTS3000 battery test system at 25°C . The cut-off voltages were 0.01 V and 3.0 V (vs. Na/Na^+). Cyclic voltammetry (CV) were performed on a CHI 760E electrochemical workstation. Electrochemical impedance spectroscopy (EIS) was carried out on a Princeton Applied Research P3000A spectrometer. The perturbation amplitude was 10 mV and the frequency range was 100 kHz to 0.01 Hz .

3. Results and discussion

The synthesis route of $\text{Fe}_3\text{Se}_4@\text{C}$ NCs is schematically illustrated in Fig. 1a. Firstly, Fe_3O_4 nanospheres with uniform size distribution was synthesized via a facile hydrothermal route and used as the precursor. In the following step, Fe_3O_4 nanospheres were coated with PDA followed by carbonization in Ar to transform $\text{Fe}_3\text{O}_4@\text{PDA}$ into $\text{Fe}_3\text{O}_4@\text{C}$ nanospheres. To form the nanocage structure, the $\text{Fe}_3\text{O}_4@\text{C}$ nanospheres were etched HCl solution for 1 h to partially remove Fe_3O_4 from the nanosphere cores, forming desired voids between the external carbon shell and the Fe_3O_4 . Finally, selenization at high temperature was performed to transfer the carbon encapsulated Fe_3O_4 to Fe_3Se_4 , resulting in $\text{Fe}_3\text{Se}_4@\text{C}$ NCs. As shown in Fig. 1b, the Fe_3O_4 nanospheres exhibit regular spherical morphology and high mono-dispersity with an average diameter of around 300 nm . After the carbon coating, HCl etching and subsequent selenization, the nano-spherical morphology is ultimately preserved in $\text{Fe}_3\text{O}_4@\text{C}$ NSs and $\text{Fe}_3\text{Se}_4@\text{C}$ NCs. As shown in Fig. S1a and b, the structural integrity of the carbon shells are well maintained in the $\text{Fe}_3\text{Se}_4@\text{C}$ NCs after the selenization process. Compared with $\text{Fe}_3\text{Se}_4@\text{C}$ NCs, the Fe_3Se_4 NSs and $\text{Fe}_3\text{Se}_4@\text{C}$ NSs show the irregularly nano-spherical morphology with a coarse surface as shown in Fig. S2a and b.

TEM was employed to further investigate the microstructure of the as-prepared samples and the results are presented in Fig. 2. As shown in Fig. 2a, the dense Fe_3O_4 core and the encapsulating carbon layer are well resolved by their distinguished difference in imaging contrast. Fig. 2b shows the carbon shell of $\text{Fe}_3\text{Se}_4@\text{C}$ is well preserved, in which

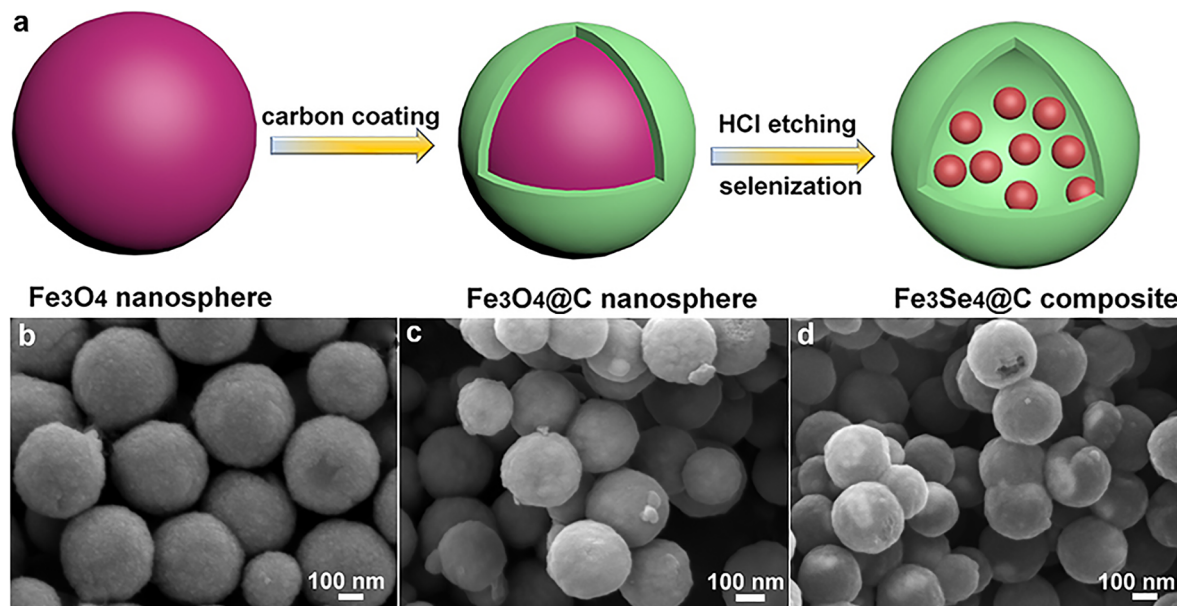


Fig. 1. (a) Schematic fabrication route of the $\text{Fe}_3\text{Se}_4@\text{C}$ NSs. (b) SEM morphology of Fe_3O_4 NSs. (c) SEM morphology of $\text{Fe}_3\text{O}_4@\text{C}$ NSs. (d) SEM morphology of $\text{Fe}_3\text{Se}_4@\text{C}$ NCs.

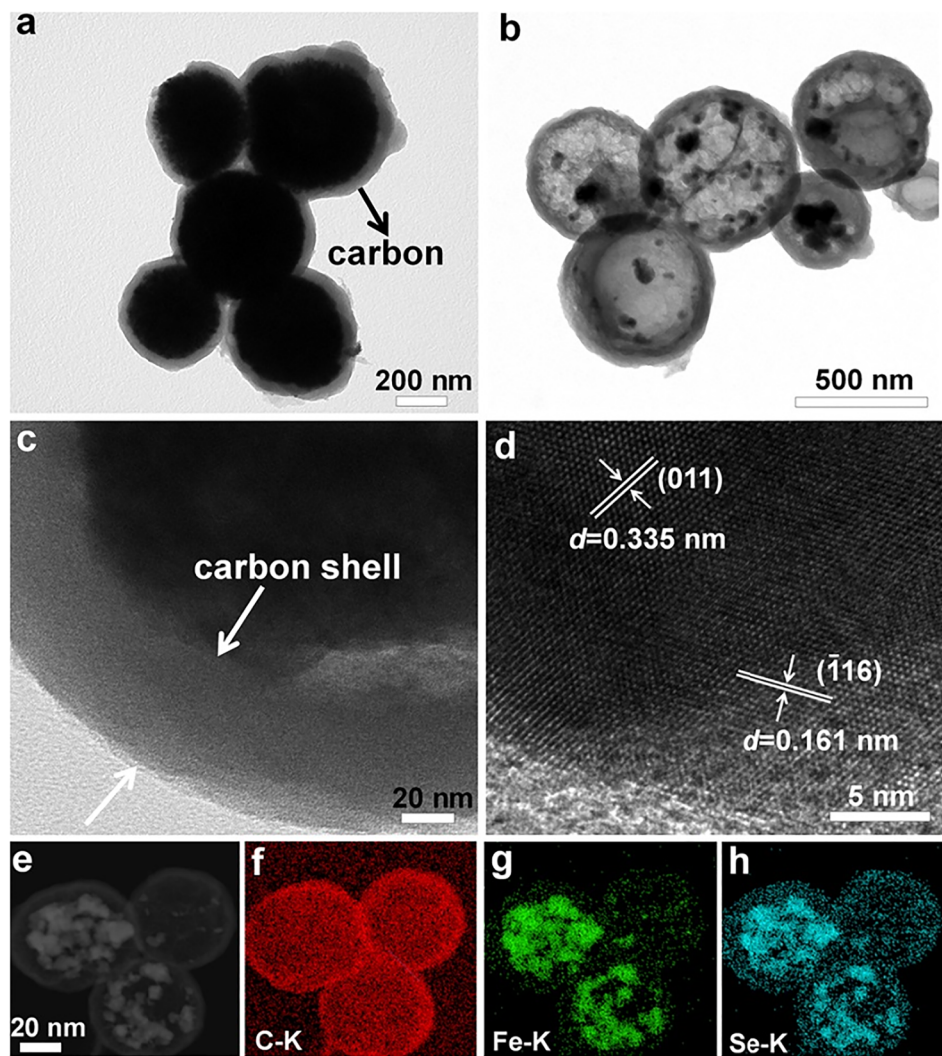


Fig. 2. (a) TEM image of the $\text{Fe}_3\text{O}_4@\text{C}$ NSs. (b-c) TEM images of the $\text{Fe}_3\text{Se}_4@\text{C}$ NCs. (d) HRTEM images of the $\text{Fe}_3\text{Se}_4@\text{C}$ NCs. (e) HAADF image of the $\text{Fe}_3\text{Se}_4@\text{C}$ NCs and its corresponding EDS elemental mappings: (f) C, (g) Fe and (h) Se.

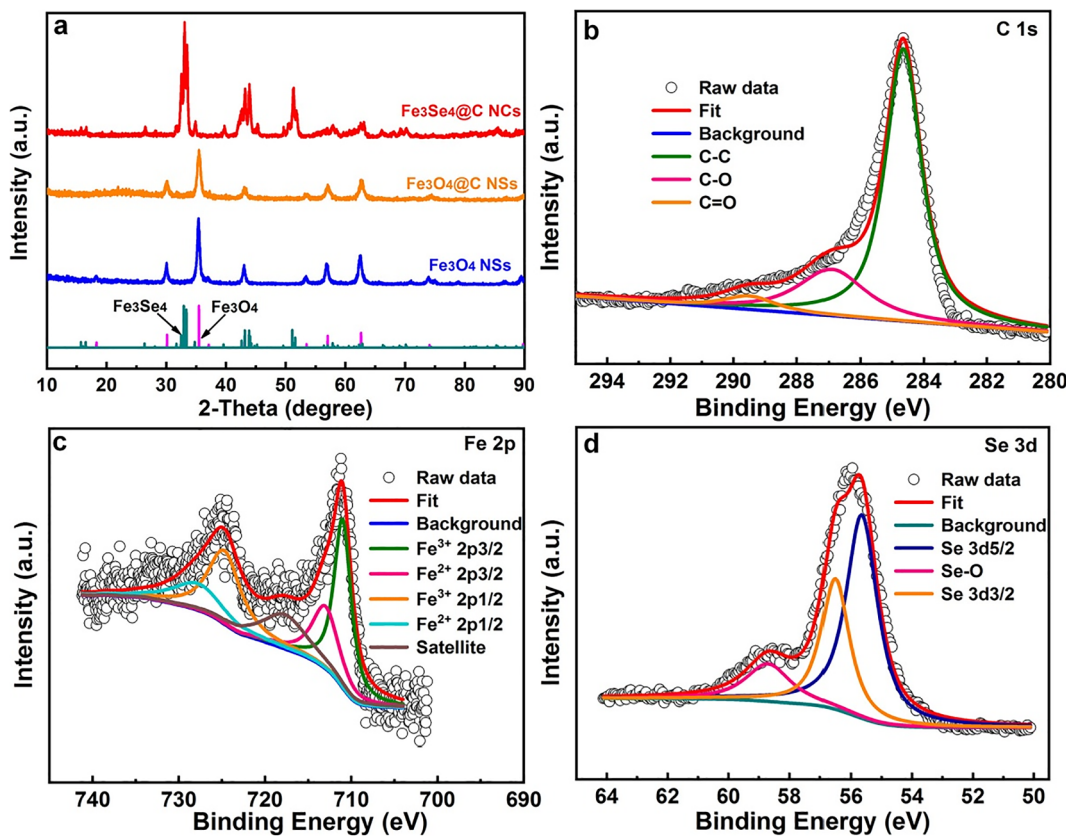


Fig. 3. (a) XRD profiles of the obtained Fe_3O_4 NSs, $\text{Fe}_3\text{O}_4@\text{C}$ NSs and $\text{Fe}_3\text{Se}_4@\text{C}$ NCs composite. Standard patterns of Fe_3O_4 (JCPDS 88-0866) and Fe_3Se_4 (JCPDS 73-2021) are also provided for comparison. (b) XPS core level spectra of (b) C 1s, (c) Fe 2p and (d) Se 3d for $\text{Fe}_3\text{Se}_4@\text{C}$ NCs.

Fe_3Se_4 nanoparticles are confined, forming a nanocage structure with a uniform diameter around 300 nm inherited from the Fe_3O_4 precursor. The thickness of the carbon shell is confirmed to be around 40 nm as shown in Fig. 2c. Voids are clearly visible between the carbon shell and the inner Fe_3Se_4 nanoparticles, which helps to effectively relieve the volume expansion upon sodiation of the Fe_3Se_4 nanoparticles. When the time is prolonged to 2 h in 3 M HCl for Fe_3O_4 , almost all the Fe_3O_4 are dissolved with the formation of the hollow carbon shell (hollow C NSs, Fig. S3). The Fe_3Se_4 (0 1 1) planes with d-spacing of 0.335 nm and the (1 1 6) planes with d-spacing of 0.161 nm are clearly observed by high-resolution TEM (HRTEM) imaging of the $\text{Fe}_3\text{Se}_4@\text{C}$ composite, as shown in Fig. 2d. Furthermore, high-angle annular dark-field (HAADF) imaging (Fig. 2e) of $\text{Fe}_3\text{Se}_4@\text{C}$ and its corresponding elemental mapping suggest continuous C (Fig. 2f) distribution on the external shell and decoration of Fe (Fig. 2g) as well as Se (Fig. 2h) in the central cores of the unique nanocages structure.

XRD was carried out to determine the phase compositions of the as-prepared bulk samples and the results are shown in Fig. 3a. Diffraction peaks located at $2\theta = 30.1, 35.4, 43.1, 57.0$ and 62.6° collected from the Fe_3O_4 nanospheres can be assigned to the cubic Fe_3O_4 phase (JCPDS 88-0866) [24]. After the carbon coating, diffraction peaks from Fe_3O_4 were remained in the $\text{Fe}_3\text{O}_4@\text{C}$ sample. The XRD peaks of the $\text{Fe}_3\text{Se}_4@\text{C}$ NCs sample match well with monoclinic Fe_3Se_4 (JCPDS 73-2021) indicating a through transformation in the selenization process and is in-line with the HRTEM observations. As shown in Fig. S4, diffraction peaks from the resulting $\text{Fe}_3\text{Se}_4@\text{C}$ NSs and Fe_3Se_4 NSs also match well with the monoclinic Fe_3Se_4 , confirming that the formed Fe_3Se_4 is not altered by the difference in their nanostructures. The external carbon shell was further characterized using Raman spectroscopy. The results from $\text{Fe}_3\text{O}_4@\text{C}$ NSs and $\text{Fe}_3\text{Se}_4@\text{C}$ NCs composites (shown in Fig. S5) both exhibit a disorder induced D band located at around 1351.6 cm^{-1} and a graphitic G band at about 1579.9 cm^{-1} ,

respectively, indicating its amorphous nature consistent with the TEM microstructure observation [25]. The mass fraction of Fe_3Se_4 in $\text{Fe}_3\text{Se}_4@\text{C}$ NCs was determined using TGA. As shown in Fig. S6a, the XRD result indicates that the residual product after calcining $\text{Fe}_3\text{Se}_4@\text{C}$ NCs in air at 950°C match well with Fe_2O_3 . The mass fraction of Fe_3Se_4 was therefore determined be 61.2% from the TGA result (Fig. S6b). In addition to the macroporous voids observed from TEM, the pore structure of $\text{Fe}_3\text{Se}_4@\text{C}$ NCs was also studied by using nitrogen adsorption and desorption at 77 K . Fig. S7 shows the obtained isotherms as well as the corresponding pore size distribution calculated using the Barrett-Joyner-Halenda (BJH) model. The existence of mesopores is confirmed by the hysteresis between the desorption and adsorption branches and the pore size distribution analysis indicates that the size of the mesopores is centered around 3.5 nm.

XPS was further conducted to investigate the chemical bonding state in the obtained $\text{Fe}_3\text{Se}_4@\text{C}$ nanocages. The survey spectrum (Fig. S6) reveals the presence of Se, Fe, O and C four elements in the $\text{Fe}_3\text{Se}_4@\text{C}$ NCs. Table S1 summarizes the binding energy states of three elements at different peak positions. In the high-resolution C 1s spectrum (Fig. 3b), deconvolution reveals the contribution from three characteristic peaks located at 289.6, 286.9 and 284.6 eV, corresponding to $\text{C}=\text{O}$ [7], $\text{C}-\text{O}$ [24], as well as sp^2 hybridized carbons ($\text{C}-\text{C}$) [24], respectively [26]. Existence of the oxygen-containing groups indicates a relatively low graphitic level of the carbon shell as a result of the modest carbonization temperature and is in-line with the TEM and Raman results. The high-resolution Fe 2p spectrum (Fig. 3c) contains two major peaks corresponding to $\text{Fe } 2\text{p}_{3/2}$ and $\text{Fe } 2\text{p}_{1/2}$ locate at 711.1 and 725.0 eV respectively, which result from the spin-orbit splitting and are intermediately by a satellite peak at around 717.8 eV [13]. Owing to the mixed valence states in Fe_3Se_4 , both the $\text{Fe } 2\text{p}_{3/2}$ and $\text{Fe } 2\text{p}_{1/2}$ peaks can be further deconvoluted to two sub-peaks Fe^{3+} ($2\text{p}_{3/2}$ around 711.0 eV, $2\text{p}_{1/2}$ around 724.9 eV) and Fe^{2+} ($2\text{p}_{3/2}$ around 713.1 eV,

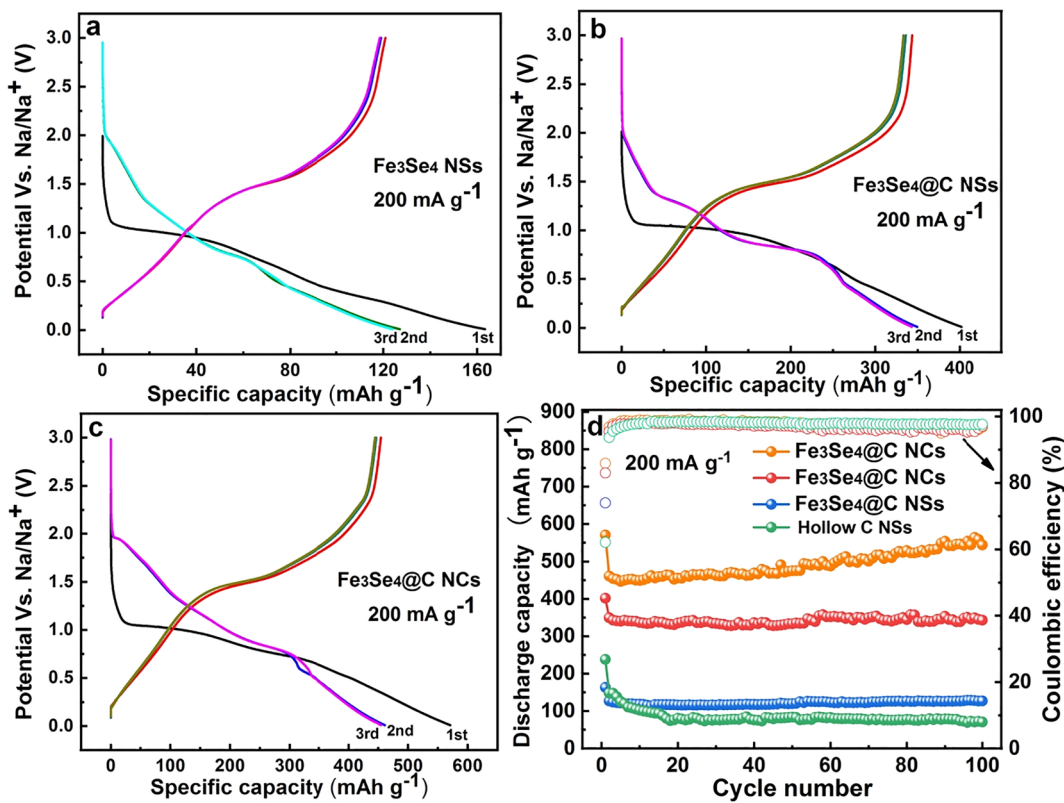


Fig. 4. Galvanostatic charge-discharge profiles of (a) Fe_3Se_4 NSSs, (b) $\text{Fe}_3\text{Se}_4@\text{C}$ NSSs and (c) $\text{Fe}_3\text{Se}_4@\text{C}$ NCs at 200 mA g^{-1} . (d) Cycling performances of the Fe_3Se_4 NSSs, $\text{Fe}_3\text{Se}_4@\text{C}$ NSSs, $\text{Fe}_3\text{Se}_4@\text{C}$ NCs and hollow C NSSs anodes at 200 mA g^{-1} .

$2p_{1/2}$ around 728.0 eV [27,28]. In the high-resolution Se 3d spectrum shown in Fig. 3d, the two main peaks centered at around 55.6 and 56.5 eV can be assigned to $\text{Se } 3d_{5/2}$ and $\text{Se } 3d_{3/2}$, respectively, in agreement with previously reported Fe_3Se_4 [22]. Meanwhile, the peak located at 58.7 eV can be assigned to Se-O bonds, which originated from the surface oxidation of selenium during the selenization process and are typically observed on selenium compounds [10,14,21]. Based above analysis, the Fe_3Se_4 nanoparticles have successfully confined in hollow carbon nanocages to form unique core-shell structure.

Galvanostatic charge-discharge tests at a low current density of 200 mA g^{-1} were first performed to study the electrochemical sodium storage performance of Fe_3Se_4 NSSs and $\text{Fe}_3\text{Se}_4@\text{C}$ NSSs in comparison with $\text{Fe}_3\text{Se}_4@\text{C}$ NCs over a potential window of 0.01–3.0 V. As shown in Fig. 4a, the Fe_3Se_4 NSSs delivered specific capacity of 163.3 mAh g^{-1} in the first cycle, followed by an irreversible capacity loss in the second cycle, only maintaining 123.9 mAh g^{-1} in the third cycle. This result indicates the lower reversibility of pure Fe_3Se_4 NSSs. After coating of the carbon layer, the initial discharge specific capacity of $\text{Fe}_3\text{Se}_4@\text{C}$ NSSs was improved to 401.8 mAh g^{-1} , with a smaller irreversible capacity loss and a reservation of 343.1 mAh g^{-1} in the third cycle (see Fig. 4b). In comparison, $\text{Fe}_3\text{Se}_4@\text{C}$ NCs exhibits a high initial discharge capacity of 570.7 mAh g^{-1} (see Fig. 4c), which is much higher than that of $\text{Fe}_3\text{Se}_4@\text{C}$ NSSs, Fe_3Se_4 NSSs and the hollow C NSSs. Furthermore, the discharge-charge profiles of the second and third cycles are well-overlapped, demonstrating superior reversibility as an SIB anode material. This improvement is primarily ascribed to the sufficient voids that exist within the nanocages structure that can effectively accommodate the large volume changes of Fe_3Se_4 upon sodiation/desodiation. In addition, the capacity contribution from the carbon shell was determined to be relatively low. As shown in Fig. S9, the hollow C NSSs electrode delivered a specific discharge capacity of 238.2 mAh g^{-1} in the first cycle, which experienced a large capacity loss in the following cycles and a retention of only 147.5 mAh g^{-1} in the third cycle.

In long-term cycling, the nanocage structure of $\text{Fe}_3\text{Se}_4@\text{C}$ NSSs better copes with the repeated volume change of Fe_3Se_4 during charge/discharge and therefore possesses vastly improved structural integrity and cycling stability. Fig. 4d shows the long-term cycling performance of Fe_3Se_4 NSSs, $\text{Fe}_3\text{Se}_4@\text{C}$ NSSs, hollow C NSSs and $\text{Fe}_3\text{Se}_4@\text{C}$ NCs anodes at 200 mA g^{-1} . The Fe_3Se_4 NSSs anode exhibits an initial specific discharge and charge capacity of 163.3 and 120.8 mAh g^{-1} , respectively, corresponding to an initial coulombic efficiency (CE) of 73.9%. In the following cycles, the Fe_3Se_4 NSSs anode experiences a gradual capacity fading and maintained the discharge specific capacity of 123.9 mAh g^{-1} at the 100th cycle. After coating with carbon, $\text{Fe}_3\text{Se}_4@\text{C}$ NSSs anode shows an initial capacity drop then experienced a gradual capacity fading and the discharge specific capacity reached 343.0 mAh g^{-1} at the 100th cycle. In contrast, a significant improvement in initial specific discharge and charge capacity is clearly evident in the $\text{Fe}_3\text{Se}_4@\text{C}$ NCs whilst its cycling stability also greatly outperforms Fe_3Se_4 NSSs and $\text{Fe}_3\text{Se}_4@\text{C}$ NSSs anode over the 100 test cycles. A gradual increase after the initial capacity drop occurred on the $\text{Fe}_3\text{Se}_4@\text{C}$ NCs anode, maintaining a reversible specific capacity of $544.1 \text{ mA h g}^{-1}$ with 99.0% CE. Meanwhile, the cycling performance of the hollow C NSSs was also investigated. The discharge capacity was 71.0 mAh g^{-1} after 100 cycles, which was significantly lower than that of the $\text{Fe}_3\text{Se}_4@\text{C}$ NCs. This indicates a substantially low capacity contribution from the carbon shell. The role of the carbon shell should be mainly attributed to its high electrical conductivity and volume-change tolerance that enabled much improved utilization of Fe_3Se_4 in $\text{Fe}_3\text{Se}_4@\text{C}$ NCs [27,28]. The rising trend of capacity during the cycling of $\text{Fe}_3\text{Se}_4@\text{C}$ NCs can be attributed to the activation process, where the structure of active Fe_3Se_4 in the composite gradually rearranged to provide more accessible active sites for the insertion of Na^+ during the cycling process.

Fig. 5a shows the cycling stability of the three anodes at further increased cycling current density of 1000 and 2000 mA g^{-1} . At 1000 mA g^{-1} , the Fe_3Se_4 NSSs anode delivered a discharge specific

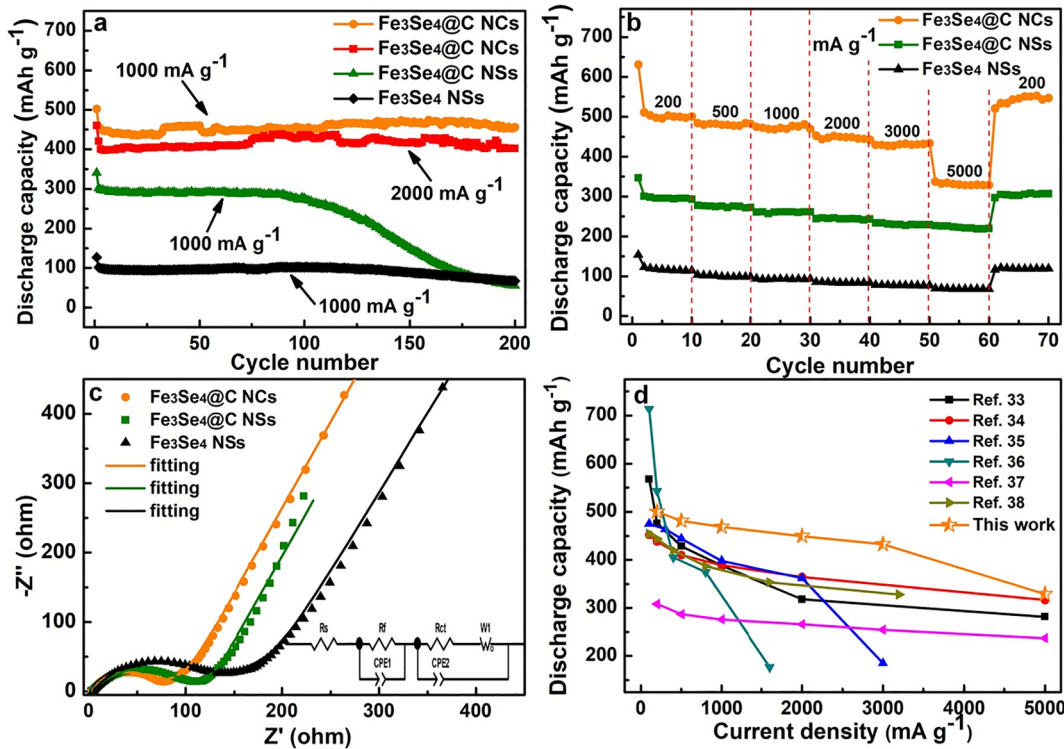


Fig. 5. (a) Long time cycling performance of the Fe_3Se_4 NSs, $\text{Fe}_3\text{Se}_4@\text{C}$ NSs, and $\text{Fe}_3\text{Se}_4@\text{C}$ NCs anodes at 1000 and 2000 mA g^{-1} . (b) Rating performance of the Fe_3Se_4 NSs, $\text{Fe}_3\text{Se}_4@\text{C}$ NSs and $\text{Fe}_3\text{Se}_4@\text{C}$ NCs anodes at increasing current densities. (c) Nyquist plots of Fe_3Se_4 NSs, $\text{Fe}_3\text{Se}_4@\text{C}$ NSs and $\text{Fe}_3\text{Se}_4@\text{C}$ NCs anodes after the rating test and Equivalent circuit model of the three electrodes. (d) Comparison of the rating capability of the $\text{Fe}_3\text{Se}_4@\text{C}$ NCs anode composite in this study with previously reported other SIBs anodes.

capacity of 127.2 mAh g^{-1} in the first cycle and faded rapidly in subsequent cycles with only 67.1 mAh g^{-1} retained after 200 cycles. By contrast, the discharge specific capacity of $\text{Fe}_3\text{Se}_4@\text{C}$ NSs anode was improved to 340.7 mAh g^{-1} at first cycle, however, the reversible capacity also faded rapidly in subsequent cycles, with only 54.7 mAh g^{-1} retained after 200 cycles. The $\text{Fe}_3\text{Se}_4@\text{C}$ NCs anode, in comparison, exhibited a much higher initial discharge capacity of 501.9 mAh g^{-1} , as well as a much better capacity retention of 90.7% relative to its first cycle, delivering a stable discharge capacity of 455.6 mAh g^{-1} after 200 cycles. Surprisingly, when the current density was raised to 2000 mA g^{-1} , $\text{Fe}_3\text{Se}_4@\text{C}$ NCs still exhibit ultra-stable cycling performance and its specific capacity remained to be above 402.2 mAh g^{-1} over 200 charge/discharge cycles.

The rating capabilities of the all anode materials were also investigated at a sequence of current densities from 200 to 5000 mA g^{-1} . As presented in Fig. 5b, the $\text{Fe}_3\text{Se}_4@\text{C}$ NCs composite performs superior than Fe_3Se_4 NSs and $\text{Fe}_3\text{Se}_4@\text{C}$ NSs anodes at all investigated current densities. At the exceptionally high current density of 5000 mA g^{-1} , the $\text{Fe}_3\text{Se}_4@\text{C}$ NSs delivers a satisfying specific capacity of 328.7 mAh g^{-1} whilst that of the Fe_3Se_4 NSs and $\text{Fe}_3\text{Se}_4@\text{C}$ NSs remain to be only 67.3 and 216.6 mAh g^{-1} , respectively. Furthermore, the specific capacity of $\text{Fe}_3\text{Se}_4@\text{C}$ NCs restores to 551.1 mAh g^{-1} when the current density was set back to 200 mA g^{-1} , delivering an even higher than initial capacity. The comparably lower rating capability of Fe_3Se_4 NSs and $\text{Fe}_3\text{Se}_4@\text{C}$ NSs can be attributed to the severe electrode polarization resulted from the lack of sufficient internal void space to accommodate the large volume changes and provide fast Na^+ diffusion channels.

To gain further insight into the origin of the superior performance of $\text{Fe}_3\text{Se}_4@\text{C}$ NCs anode, EIS was performed on the anode materials after the rating test. As presented in Fig. 5c, Nyquist plots of three anodes all exhibit a depressed semicircle in the high frequency region, which originates from the anode internal resistance. The sloping line in the low frequency region can be attributed to the process of Na^+ diffusion

into the anode active materials from the electrolyte. The EIS results were analysed by fitting the Nyquist plots using an equivalent circuit model and the fitted spectra are also shown in Fig. 5c. In the equivalent circuit model, R_s is the resistance of the electrolyte and cell components [29]. R_f indicates the resistance related to the surface film and SEI surface on the electrode. R_{ct} reflects the charge transfer impedance at the electrolyte/surface film/electrode interfaces [30,31]. CPE is the constant phase element, and W_1 refers to Warburg impedance which reflects the Na^+ transfer process [32]. The obtained R_s , R_f , and R_{ct} values are summarized in Table S2. The $\text{Fe}_3\text{Se}_4@\text{C}$ NCs anode exhibits relatively smaller R_{ct} and R_f than Fe_3Se_4 NSs and $\text{Fe}_3\text{Se}_4@\text{C}$ NSs anodes. This can be attributed to the intact carbon shell of $\text{Fe}_3\text{Se}_4@\text{C}$ NCs with voids and Fe_3Se_4 in its confined space that stabilizes the inter-particle contact resistance, leading to vastly improved sodium storage performance. Additionally, it is noteworthy that the rating capability of the $\text{Fe}_3\text{Se}_4@\text{C}$ NCs composite from this study outperforms for most previously reported anode materials for SIBs. As summarized in Fig. 5d and Table S3 [21,22,33–36], the specific capacity of $\text{Fe}_3\text{Se}_4@\text{C}$ NCs composite at low and high current densities are among the highest reported in the literature whilst the capacity loss with increasing current density is among the narrowest. Its superior performance can be ascribed to following reasons. Firstly, the Fe_3Se_4 nanoparticles are closely confined in hollow carbon nanocages that prevent the aggregation of Fe_3Se_4 nanoparticles and facilitate their uniform dispersion during material synthesis. Secondly, the rationally designed void space between the carbon shell and Fe_3Se_4 nanoparticles allows for the free expansion of Fe_3Se_4 without deforming the carbon shell, therefore preventing structural pulverization during charge/discharge process. The voids between the confined Fe_3Se_4 nanoparticles also help to shorten the diffusion length of Na^+ , enabling improved specific capacity at high current densities. Finally, the carbon shell possesses high electronical and ionic conductivity that provide fast electron and Na^+ transportation during the intense anode electrochemical transformation

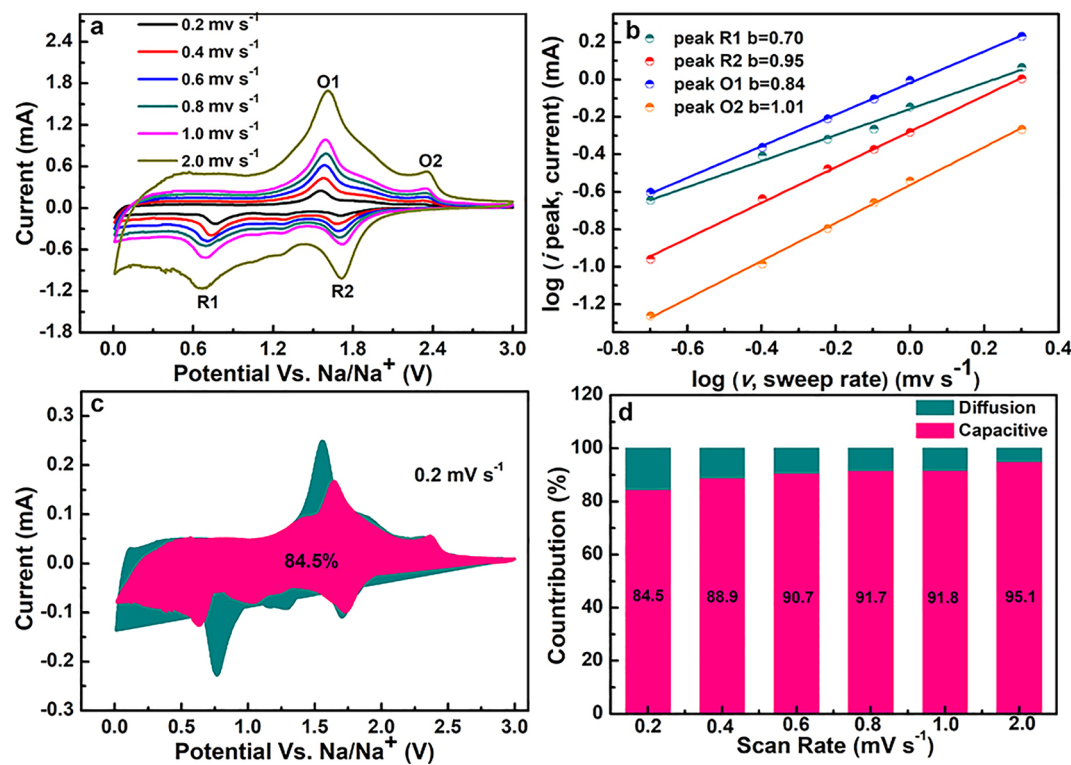


Fig. 6. (a) CV curves of the Fe₃Se₄@C NCs anode at elevating scan rates. (b) Linear fitting of the log (*i*) versus log (*v*) plots for the three anodic and cathodic peaks of O1, O2, R1 and R2. (c) Capacitive contribution (red) in the CV curve of the Fe₃Se₄@C NCs anode in comparison to its total current at 0.2 mV s⁻¹. (d) Calculated capacitive and diffusion contributions for the specific capacity of Fe₃Se₄@C NCs anode at various scan rates.

whilst help to form a stable solid-electrolyte-interphase (SEI) layer on the anode surface [37–39].

To investigate the capacity contributions of the Fe₃Se₄@C NCs as SIBs anodes, CV measurements at different scan rates were performed. Fig. 6a shows the CV curves of Fe₃Se₄@C NCs collected at scan rates from 0.02 to 2.0 mV s⁻¹. The overall shape of all CV curves are maintained at increasing scan rates, implying minor polarization along with elevating current densities applied to the anode. Peak current *i* and scan rate *v* follow the Power Law of $i = av^b$. The *b* values correspond to the slopes in the plots of $\log(v)$ versus $\log(i)$, as shown in Fig. 6b. The oxidation peaks (denoted as O1 peak at 1.60 V and O2 at 2.34 V) and reduction peaks (denoted as R1 at 0.65 V and R2 at 1.70 V) are chosen for the calculations. *b* values close to 1.0 indicates a surface-controlled electrochemical reaction, while the *b* close to 0.5 suggests a diffusion-controlled process [40]. As shown in Fig. 6b, the calculated *b*-values of Peaks O1, O2, R1, and R2 are 1.01, 0.84, 0.70 and 0.95 respectively. This suggests that electrochemical energy storage in the Fe₃Se₄@C NCs composite is mainly a surface-controlled process, involving a fast Na⁺ insertion/extraction reaction.

Contributions from pseudocapacitive (k_1v) energy storage and diffusion-controlled intercalation ($k_2v^{1/2}$) are further calculated quantitatively using the following equation [41]:

$$i(v) = k_1v + k_2v^{1/2}$$

where $i(v)$ is the measured current at a fixed potential, v indicates the scan rate and both k_1 and k_2 are adjustable parameters. As presented in Fig. 6c and d, at the lowest scan rate of 0.2 mV s⁻¹, the capacitive-controlled contribution exhibits a high value 84.5%. Along with increasing scan rates, it further increases and reached 95.1% at the scan rate of 2 mV s⁻¹ whilst the diffusion contribution continuously decreases. The result further demonstrates the fast Na⁺ transportation kinetics within the Fe₃Se₄@C NCs and its structural stability to withstand the associated rapid mass transfer, which together leads to its superior sodium storage performance.

4. Conclusion

A Fe₃Se₄@C NCs nanocage composite consisting of Fe₃Se₄ nanoparticles surrounded and protected by a conductive carbon shell have been successfully synthesized using a facile etching method followed by a selenization process. Excellent rating capability and high cycling stability are achieved simultaneously on the Fe₃Se₄@C NCs anode. The thin and self-supporting carbon shells help to prevent the aggregation of the Fe₃Se₄ nanoparticles whilst enhance the conductivity of the sodium storage composite. Moreover, rationally designed void space in between the carbon shell and Fe₃Se₄ nanoparticles successfully confines the volume change of Fe₃Se₄ nanoparticles to avoid deforming the composite nanostructure during the charge/discharge process. Owing to these unique structural features, the as-prepared Fe₃Se₄@C NCs composite exhibits high reversible capacity, superior rating capability and excellent cycling stability. These advantages on top of its scalable synthesis mean that the Fe₃Se₄@C NCs holds a promising application potential as anode materials in future SIBs.

CRediT authorship contribution statement

Jiajia Ye: Methodology, Investigation, Writing - review & editing, Writing - original draft. **Zhiqiang Zheng:** Conceptualization. **Guang Xia:** Conceptualization. **Cheng Hu:** Resources, Writing - review & editing, Supervision, Data curation.

Acknowledgments

This work was financially supported by The Natural Science Foundation of Jiangsu Province (BK20180229), The Natural Science Foundation of Shandong Province (ZR2019QEM001) and The Fundamental Research Funds of Shandong University (2018JC038). The authors would like to thank Yankai Li from Shiyanjia Lab for the support of XPS analysis (www.shiyanjia.com).

Appendix A. Supplementary material

Supplementary data to this article can be found online at <https://doi.org/10.1016/j.apsusc.2020.146260>.

References

- [1] S.H. Yang, S. Park, Y.C. Kang, Mesoporous CoSe₂ nanoclusters threaded with nitrogen-doped carbon nanotubes for high-performance sodium-ion battery anodes, *Chem. Eng. J.* 370 (2019) 1008–1018.
- [2] W. Ren, H. Zhang, C. Guan, C. Cheng, Ultrathin MoS₂ nanosheets@metal organic framework-derived N-doped carbon nanowall arrays as sodium ion battery anode with superior cycling life and rate capability, *Adv. Funct. Mater.* 27 (2017) 1702116.
- [3] Y. Jiang, Y. Wu, Y. Chen, Z. Qi, J. Shi, L. Gu, Y. Yu, Design nitrogen (N) and sulfur (S) Co-doped 3D graphene network architectures for high-performance sodium storage, *Small* 14 (2018) 1703471.
- [4] L. Kong, J. Zhu, W. Shuang, X. Bu, Nitrogen-doped wrinkled carbon foils derived from MOF nanosheets for superior sodium storage, *Adv. Energy Mater.* 8 (2018) 1801515.
- [5] M. Ren, H. Xu, F. Li, W. Liu, C. Gao, L. Su, G. Li, J. Hei, Sugarapple-like N-doped TiO₂ @carbon core-shell spheres as high-rate and long-life anode materials for lithium-ion batteries, *J. Power Sources* 353 (2017) 237–244.
- [6] B. Ahmed, D.H. Anjum, Y. Gogotsi, H.N. Alshareef, Atomic layer deposition of SnO₂ on MXene for Li-ion battery anodes, *Nano Energy* 34 (2017) 249–256.
- [7] J. Liu, L. Yu, C. Wu, Y. Wen, K. Yin, F. Chiang, R. Hu, J. Liu, L. Sun, L. Gu, J. Maier, Y. Yu, M. Zhu, New nanoconfined galvanic replacement synthesis of hollow Sb@C yolk-shell spheres constituting a stable anode for high-Rate Li/Na-ion batteries, *Nano Lett.* 17 (2017) 2034–2042.
- [8] J. Qin, D. Liu, N. Zhao, C. Shi, E. Liu, F. He, L. Ma, Q. Li, J. Li, C. He, Fabrication of Sn-core/CNT-shell nanocable anchored interconnected carbon networks as anode material for lithium ion batteries, *Mater. Lett.* 212 (2018) 94–97.
- [9] Z. Huang, H. Hou, Y. Zhang, C. Wang, X. Qiu, X. Ji, Layer-tunable phosphorene modulated by the cation insertion rate as a sodium-storage anode, *Adv. Mater.* 29 (2017) 1702372.
- [10] K. Zhang, M. Park, L. Zhou, G. Lee, W. Li, Y. Kang, J. Chen, Urchin-like CoSe₂ as a high-performance anode material for sodium-ion batteries, *Adv. Funct. Mater.* 26 (2016) 6728–6735.
- [11] Y. Tang, Z. Zhao, X. Hao, Y. Wang, Y. Liu, Y. Hou, Q. Yang, X. Wang, J. Qiu, Engineering hollow polyhedrons structured from carbon-coated CoSe₂ nanospheres bridged by CNTs with boosted sodium storage performance, *J. Mater. Chem. A* 5 (2017) 13591–13600.
- [12] H. Fan, H. Yu, X. Wu, Y. Zhang, Z. Luo, H. Wang, Y. Guo, S. Madhavi, Q. Yan, Controllable preparation of square nickel chalcogenide (NiS and NiSe₂) nanoplates for superior Li/Na ion storage properties, *ACS Appl Mater Inter* 8 (2016) 25261–25267.
- [13] K. Zhang, Z. Hu, X. Liu, Z. Tao, J. Chen, FeSe₂ microspheres as a high-performance anode material for Na-ion batteries, *Adv. Mater.* 27 (2015) 3305–3309.
- [14] W. Zhao, C. Guo, C.M. Li, Lychee-like FeS₂@FeSe₂ core-shell microspheres anode in sodium ion batteries for large capacity and ultralong cycle life, *J. Mater. Chem. A* 5 (2017) 19195–19202.
- [15] H. Liu, H. Guo, B. Liu, M. Liang, Z. Lv, K.R. Adair, X. Sun, Few-layer MoSe₂ nanosheets with expanded (002) planes confined in hollow carbon nanospheres for ultrahigh-performance Na-ion batteries, *Adv. Funct. Mater.* 28 (2018) 1707480.
- [16] J. Yue, Q. Sun, Z. Fu, Cu₂Se with facile synthesis as a cathode material for rechargeable sodium batteries, *Chem. Commun.* 49 (2013) 5868.
- [17] A. Pan, J. Liu, J. Zhang, W. Xu, G. Cao, Z. Nie, B.W. Arey, S. Liang, Nano-structured Li₃V₂(PO₄)₃/carbon composite for high-rate lithium-ion batteries, *Electrochim. Commun.* 12 (2010) 1674–1677.
- [18] J. Song, P. Yan, L. Luo, X. Qi, X. Rong, J. Zheng, B. Xiao, S. Feng, C. Wang, Y. Hu, Y. Lin, V.L. Sprenkle, X. Li, Yolk-shell structured Sb@C anodes for high energy Na-ion batteries, *Nano Energy* 40 (2017) 504–511.
- [19] Y. Zhang, J. Yang, Y. Zhang, C. Li, W. Huang, Q. Yan, X. Dong, Fe₂O₃/SnS₂ hexagonal nanoplates as lithium-ion batteries anode, *ACS Appl Mater Inter* 10 (2017) 12722–12730.
- [20] X. Tong, F. Zhang, G. Chen, X. Liu, L. Gu, Y. Tang, Core-shell aluminum@carbon nanospheres for dual-ion batteries with excellent cycling performance under high rates, *Adv. Energy Mater.* 8 (2018) 1701967.
- [21] H. Fan, H. Yu, Y. Zhang, J. Guo, Z. Wang, H. Wang, N. Zhao, Y. Zheng, C. Du, Z. Dai, Q. Yan, J. Xu, 1D to 3D hierarchical iron selenide hollow nanocubes assembled from FeSe₂@C core-shell nanorods for advanced sodium ion batteries, *Energy Storage Mater.* 10 (2018) 48–55.
- [22] Y. Lan, J. Zhou, K. Xu, Y. Lu, K. Zhang, L. Zhu, Y. Qian, Synchronous synthesis of Kirkendall effect induced hollow FeSe₂/C nanospheres as anodes for high performance sodium ion batteries, *Chem. Commun.* 54 (2018) 5704–5707.
- [23] M. Sen Bishwas, R. Das, P. Poddar, Large increase in the energy product of Fe₃Se₄ by Fe-site doping, *J. Phys. Chem. C* 118 (2014) 4016–4022.
- [24] B. Jing, S. You, Y. Ma, Z. Xing, H. Chen, Y. Dai, C. Zhang, N. Ren, J.L. Zou, Fe₃Se₄/FeSe heterojunctions in cornstalk-derived N-doped carbon framework enhance charge transfer and cathodic oxygen reduction reaction to boost bio-electricity generation, *Appl. Catal. B* 244 (2019) 465–474.
- [25] Z. Wan, J. Shao, J. Yun, H. Zheng, T. Gao, M. Shen, Q. Qu, H. Zheng, Core-shell structure of hierarchical quasi-hollow MoS₂ microspheres encapsulated porous carbon as stable anode for Li-ion batteries, *Small* 10 (2014) 4975–4981.
- [26] Y. He, L. Wang, C. Dong, C. Li, X. Ding, Y. Qian, L. Xu, In-situ rooting ZnSe/N-doped hollow carbon architectures as high-rate and long-life anode materials for half/full sodium-ion and potassium-ion batteries, *Energy Storage Mater.* 23 (2019) 35–45.
- [27] J. Ye, Q. Hao, B. Liu, Y. Li, C. Xu, Facile preparation of graphene nanosheets encapsulated Fe₃O₄ octahedra composite and its high lithium storage performances, *Chem. Eng. J.* 315 (2017) 115–123.
- [28] J.J. Ye, Z. Wang, Q. Hao, B. Liu, C.X. Xu, Facile fabrication of Fe₃O₄ octahedra/nanoporous copper network composite for high-performance anode in Li-Ion batteries, *J. Colloid Interf. Sci.* 493 (2017) 171–180.
- [29] Q. Hao, J. Wang, C. Xu, Facile preparation of Mn₂O₄ octahedra and its long-term cycle life as anode material for Li-ions batteries, *J. Mater. Chem. A* 2 (2013) 87–93.
- [30] C.X. Xu, Q. Hao, D.Y. Zhao, Facile fabrication of a nanoporous Si/Cu composite and its application as a high-performance anode in lithium-ion batteries, *Nano Res.* 9 (2016) 908–916.
- [31] Q. Hao, D.Y. Zhao, C.X. Xu, Si/Ag composite with bimodal micro-nano porous structure as a high-performance anode for Li-ion batteries, *Nanoscale* 7 (2015) 5320–5327.
- [32] Q. Hao, Y. Yu, D. Zhao, C.X. Xu, Composited Co₃O₄/Ag with flower-like nanosheets anchored on a porous substrate as a high-performance anode for Li-ion batteries, *J. Mater. Chem. A* 3 (2015) 15944–15950.
- [33] Y. Fang, X. Yu, X.W.D. Lou, Formation of hierarchical Cu-doped CoSe₂ microboxes via sequential ion exchange for high-performance sodium-ion batteries, *Adv. Mater.* 30 (2018) 1706668.
- [34] X. Ge, Z. Li, L. Yin, Metal-organic frameworks derived porous core/shellCoP@C polyhedrons anchored on 3D reduced graphene oxide networks as anode for sodium-ion battery, *Nano Energy* 32 (2017) 117–124.
- [35] Y. Fang, X. Yu, X.W. Lou, Bullet-like Cu₉S₅ hollow particles coated with nitrogen-doped carbon for sodium-ion batteries, *Angew. Chem. Int. Ed.* 58 (2019) 7744–7748.
- [36] A. Jin, M. Kim, K. Lee, S. Yu, Y. Sung, Spindle-like Fe₇S₈/N-doped carbon nano-hybrids for high-performance sodium ion battery anodes, *Nano Res.* 12 (2019) 695–700.
- [37] Z.M. Liu, T.C. Lu, T. Song, X.Y. Yu, X.W. Lou, U.Y. Paik, Structure-designed synthesis of FeS₂@C yolk-shell nanoboxes as a high-performance anode for sodium-ion batteries, *Energy Environ. Sci.* 10 (2017) 1576–1580.
- [38] X. Xu, Y. Dai, J. Yu, L. Hao, Y. Duan, Y. Sun, Y. Zhang, Y. Lin, J.L. Zou, Metallic state FeS anchored (Fe)/Fe₃O₄/N-doped graphitic carbon with porous sponge like structure as durable catalysts for enhancing bioelectricity generation, *ACS Appl. Mater. Inter.* 9 (2017) 10777–10787.
- [39] M. Ma, Y. Dai, J.L. Zou, L. Wang, K. Pan, H. Fu, Synthesis of iron oxide/partly graphitized carbon composites as a high-efficiency and low-cost cathode catalyst for microbial fuel cells, *ACS Appl. Mater. Inter.* 6 (2014) 13438–13447.
- [40] S. Zhu, Q. Li, Q. Wei, R. Sun, X. Liu, Q. An, L.Q. Mai, NiSe₂ Nanoctahedra as an anode material for high-rate and long-life sodium-ion battery, *ACS Appl. Mater. Inter.* 9 (2016) 311–316.
- [41] P. Ge, X. Cao, H. Hou, S. Li, X. Ji, Rodlike Sb₂Se₃ wrapped with carbon: the exploring of electrochemical properties in sodium-ion batteries, *ACS Appl. Mater. Inter.* 9 (2017) 34979–34989.